A Compliant Self-stabilization Nanopositioning Device with Modified Active-passive Hybrid Vibration Isolation Strategy

Zhongyuan Zhu, Hui Tang, *Member, IEEE*, Yunwei Huang, Zhihang Lin, Yanling Tian, Peng Yu, Chanmin Su

Abstract—Micro/mini LED (Light-emitting Diodes) display panel inspection and repairs have a high demand for vibration isolating devices to protect industrial-level atomic force microscopes (AFM scanning head) against vibrations. The motivation of this work is to combine the advantages of both passive and active vibration isolation strategies to improve inspection performance. The developed self-stabilization device achieves this objective with a design that incorporates a suspension-type passive vibration isolation unit and integrates it with the modified active-passive hybrid (MAPH) vibration isolation strategy using piezoelectric ceramics (PZT) and voice coil motors (VCM) as compensators. First, the design, modeling, and optimization of a self-stabilization device are presented based on the MAPH vibration isolation strategy. To satisfy the requirements of vibration isolation performance and a lightweight design, a multi-objective optimization task was conducted. Next, a tailor-made double compensating PID (DCPID) controller was designed to allow this mechanism run in the MAPH method to effectively isolate vibrations. Finally, a series of validation experiments, including passive vibration isolation performance tests and MAPH closed-loop tests were applied. From 1-500Hz, more than 98% frequency domain achieved a vibration isolation rate of 90%, the vibration amplification effect of the passive vibration isolation was significantly suppressed, the steady-state positioning accuracy reached ±0.1μm, load capacity was up to 2.5kg, the attenuation ratio of the disturbances reached up to 70%, and the heat of the VCM was effectively reduced. All results comprehensively confirmed that the developed compliant MAPH vibration isolation system has achieved a satisfactory self-stabilization function.

Z. Zhu, H. Tang, Y. Huang, Z. Lin are with State Key Laboratory of Precision Electronic Manufacturing Technology and Equipment, Guangdong University of Technology, Guangzhou 510006, China, and H. Tang is also with School of Engineering, University of Warwick; Y. Tian is with School of Engineering, University of Warwick, Coventry, United Kingdom; Peng Yu and Chanmin Su are with State Key Laboratory of Robotics, Shenyang Institute of Automation, Chinese Academy of Sciences (CAS), Shenyang 110016, China (e-mail: 2112001025@mail2.gdut.edu.cn; Huitang@gdut.edu.cn; 2112101327@mail2.gdut.edu.cn; lzh_hi@gdut.edu.cn; y.tian.1@warwick.ac.uk; yupeng@sia.cn; qmsu@sia.cn).
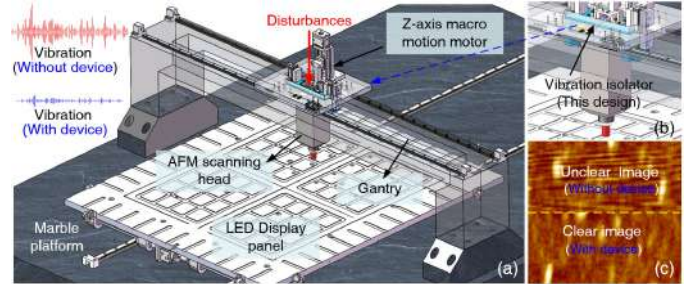
Fig. 1. The diagram of an ultra-HD display panel surface inspection system with AFM scanning head. (a) the components of the whole system; (b) the proposed compliant vibration isolation device; (c) unclear AFM image: without the developed device vs. clear AFM image: with the developed device.

Index Terms—Flexure, compliant mechanism, AFM scanning head, vibration isolation, Micro/mini LED.

I. Introduction

In the ultra-HD display era, Micro/mini LED chips on display panels are becoming extremely tiny ($\leq 10\mu m$), and total chip quantity is growing to the tens of millions merely on a 4K TV (e.g. 75 inch). To ensure production yields, the LED display panel should be inspected carefully by high-precision instruments to ensure their 3D surface physical properties are up to standards [1]–[3]. Hence, various high-precision inspection equipment, like the atomic force microscope (AFM) system, is expected to be applied to industrial production. Unfortunately, it is difficult to achieve large-scope ($\geq 1m$) display panel inspections since the workspace of the AFM scanning head is only several micrometers (see Fig. 1). Therefore, the solution is that the AFM scanning head is mounted on the gantry and carried from one point to another to inspect surfaces. However, some vibrations along the z-axis are commonly caused by the gantry and the macro motion motor because of the complex noise in the production line environment. It has a severely negative effect on the inspection performance of the AFM because of its unique working principle. Thus, finding a method to ensure that the AFM inspection equipment works in a stable and reliable condition has become an important issue for Micro/mini LED display panel inspection.

To cater to this requirement, various pioneering studies have been conducted to eliminate vibrations. Generally, they can be grouped into three categories:

1) *Pure passive vibration isolation*: Consists of a payload, a spring, and a damper [4]–[6]. It can easily achieve high-efficiency vibration isolation in the high-frequency range, while there is a resonance phenomenon (vibration amplification) in the low-frequency range;

2) *Pure active vibration isolation*: The essence is actuating the output plant to cancel out the disturbances measured by sensors [7]–[14]. Although various modern control elements were added to the controller [15]–[18], the pure active vibration isolation performance in the high-frequency range is still limited by the inherent time delay of the sensor and drive capability of the actuator;

3) *Semi-passive vibration isolation*: Semi-passive vibration isolation is different from passive vibration isolation in that it has an active component. This component identifies the type of vibration and adjusts the passive isolation mechanism for better isolation under different conditions. Unlike pure active vibration isolation, the active component in semi-passive isolation does not directly generate counteracting force [19]–[26]. Semi-passive vibration isolation still faces two issues. The first is that disturbance identification is too slow. The second is that changing physical properties is too slow to handle complicated vibrations.

Obviously, the passive and active vibration isolation strategies have their own advantages at different frequency ranges. To fully combine these advantages, designing and implementing active-passive hybrid (APH) vibration isolation has become a focus in this field [27]. In [28]–[31], the vibration isolation mechanisms are optionally driven by VCM and PZT actuators, the minimum steady-state error has achieved $\pm0.01\mu$m, and the maximum payload has reached 20 kg. However, it is hard to achieve high positioning accuracy, high bandwidth, and heavy payloads simultaneously. By the way, the VCM overheat problem has also limited its further development and application, especially when the VCM needs to continuously push or pull something. The heat will accumulate during this time and will inefficiently dissipate due to poor heat conduction, which causes the coil to easily become charred in actual production.

To solve this problem, a novel self-stabilization nanopositioning device with the MAPH vibration isolation strategy is proposed. Furthermore, a DCPID controlling strategy is designed and demonstrated in detail, which allows the system work in a MAPH vibration isolation way. Finally, a series of validation experiments were successfully implemented. The vibration attenuation rate out of the resonance region (Working frequency:$\leq$ 500Hz) can achieve 90% or more. The influence of the vibration amplification effect of the passive vibration isolation unit has been significantly inhibited. The steady-state positioning accuracy achieves up to $\pm0.1\mu$m. In the presence of step change aperiodic disturbance, the attenuation ratio of the disturbances achieves up to 70%. All the simulation and experimental results validated that the proposed MAPH self-stabilization device can achieve a satisfactory vibration isolation effect.

The main contribution of this work is the innovative design and controlling tests of a compliant self-stabilization nanopositioning device with the MAPH vibration isolation strategy,
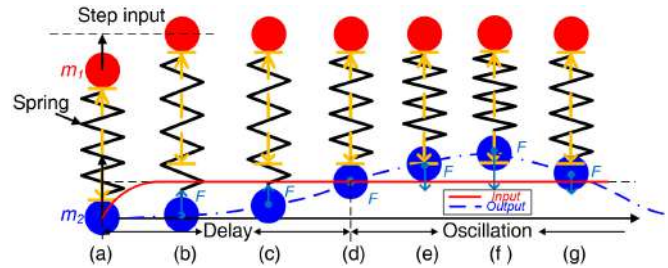

Fig. 2. The schematic diagram of displacement response using the passive vibration isolation strategy.

which would allow the industrial-level AFM inspection equipment to operate in a stable and reliable condition. The rest of this paper is organized as: In Section II, the design and modeling of the self-stabilization nanopositioning device are demonstrated; Section III is related to mechanism optimization and FEA analyses; in Section IV, a DCPID controlling strategy is designed and illustrated in detail; in Section V, a series of validation experiments and performance evaluations are conducted; finally, the achievements, as well as further work, are discussed and indicated in Section VI.

II. DESIGN AND MODELING OF THE SELF-STABILIZATION NANOPOSITIONING DEVICE

The main purpose of this section is to explore the process of passive and active vibration isolation separately and to find the method to establish the MAPH vibration isolation strategy. Based on this strategy, the detailed configuration of the device is demonstrated. For a better understanding and further control of the device, the compliance model and dynamics model are also presented.

A. Modified Active-Passive Hybrid Vibration Isolation Strategy

First, the essence of active vibration isolation is that the actuator drives the target (which weighs several kilograms) to move in the reverse trajectory along the vibration. However, with the increments in the frequency of the vibration disturbance, the inherent sensor time delay will become obvious, which means that the vibration disturbance has affected the target before it was detected. Moreover, driving this target at such a high frequency requires high driving force and large quantity of power, which easily causes the actuator saturation. Therefore, a passive vibration method is wisely adopted to handle high-frequency vibration disturbances since improving the performance of the sensor and the actuator is costly and difficult.

As mentioned earlier, the passive vibration isolation strategy cannot minimize low-frequency vibrations and has a resonance problem. However, if the input of the passive vibration isolation unit is zero, then the output is zero as well. Therefore, it needs a light movable object, whose variation in positioning can be maintained at zero under the effect of the low-frequency vibrations. It is achievable because when the vibrations are at a low frequency, the time delay of the sensor can be ignored. Therefore, the light movable object can be moved rapidly in reverse along the vibration trajectory (nullifying the
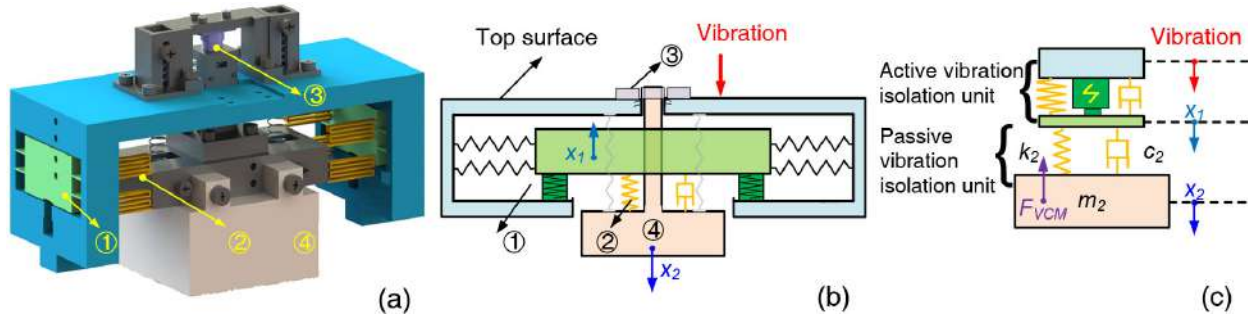
Fig. 3. 3D design drawings of the MAPH vibration isolation device. (a) assembly diagram including: 1) Active vibration isolation unit (PZT actuated), 2) Passive vibration isolation unit, 3) VCM actuator, 4) AFM scanning head; (b) transitional dynamic model (c) dynamic model.

vibration). Taking this position as the input of the passive vibration isolation mechanism, the output will be near zero when encountering low-frequency vibrations. Of course, the resonant frequency should be designed for a low frequency. The lower the resonant frequency, the better the low-frequency vibration can be eliminated by active vibration isolation.

Except for vibration elimination, closed-loop position tracking is needed. As shown in Fig. 2, (a)-(c) the m_2 has an obvious delay between input and output because of the insufficient force. As Fig.2 (d)-(g) indicates, the m_2 achieves the desired position, however, it can not remain there, and some oscillation occurs. All these issues are caused by the weak connection. The connection, i.e., the flexure spring, is too weak to provide a force large enough, and it cannot adjust promptly. Thus, a controlled force provider should be included to improve dynamic performance.

The conventional APH vibration isolation strategy usually only uses the force of VCM to control the output position. However, it is hard for a VCM to have a large driving force and a great resolution simultaneously. Therefore, it is difficult to achieve high steady-state positioning accuracy using the APH vibration isolation strategy. What makes our strategy special is that the position input ultimately affects the output, while the force in our strategy is just assistance. As a result, the position of our device can achieve high steady-state positioning accuracy because its input, the position, can be precisely controlled. To summarize, the proposed MAPH vibration isolation strategy can achieve higher steady-state positioning accuracy and large load capacity simultaneously.

B. Design of Self-Stabilization Nanopositioning Device

Based on the MAPH vibration isolation strategy, as shown in Fig. 3(a), a 3D model of the device is established. The device mainly consists of two parts, i.e., the active vibration isolation part and the passive vibration isolation part. 1) An S-shaped flexure structure (the orange part) was specially designed and acts as a spring. It connects the target (AFM scanning head) and the terminal (the light green part) of the active vibration isolation unit. These three are the components of a passive vibration isolation unit. 2) An active vibration isolation unit consists of a terminal mass (the light movable object), a high rigidity flexure spring, a piezoelectric stack (a kind of Pb-based Lanthanumdoped Zirconate Titanates (PZT) actuator), and the foundation of the piezoelectric stack. The
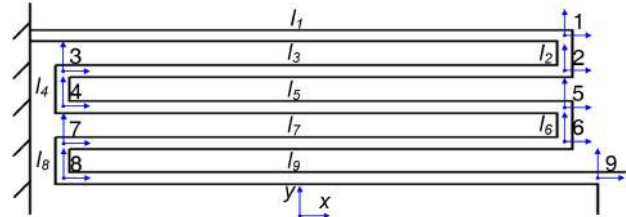
Fig. 4. Partially enlarged view of the quarter flexure structure (Link1).

position of the mass is the output of the active vibration isolation unit. Indeed, the passive vibration isolation unit and the active vibration unit share the mass (light green part) together, so the output of the active vibration isolation unit is the input of the passive vibration isolation. Finally, two active vibration isolation units are arranged on the left and right sides of the passive vibration isolation symmetrically.

Fig. 3(b) is a transitional model for a better understanding of the relevance between the dynamic model in Fig. 3(c) and the 3D model in Fig. 3(a). The top surface of the device connects to the macro motion motor which is installed on the gantry firmly and the foundation of the piezoelectric stack is connected to the top surface rigidly.

C. Device Working Principle

The vibration elimination process is demonstrated below based on the dynamic model. From the top down, the vibration first passes through the active vibration isolation unit and affects the position of the light and movable mass x_1. Then x_1 passes through the passive vibration isolation unit and affects x_2, which is the position of the AFM scanning head. Thanks to the passive vibration isolation unit, the high-frequency vibration is stabilized, because x_2 has no response to that kind of vibration at x_1. Then only the low-frequency vibration at x_1 needs to be careful. It is rejected by the active vibration isolation unit. Treating the vibration at x_1 as an output disturbance and using the powerful piezoelectric stack as the actuator, the active vibration isolation unit can reject disturbances rapidly, because the controller gain of the active vibration isolation unit is permitted to be set at a high value. Therefore, the low-frequency vibration will not occur on x_1. As a result, all vibrations are stabilized by the device, and cannot affect the position of the AFM scanning head. In addition, a VCM is added to apply force to the AFM scanning head directly, which can further improve the dynamic performance of the device as mentioned above. Two groups

Fig. 5. Overall view of the flexible hinge of the passive vibration isolation unit.

of displacement sensors are needed for measuring x_1 and x_2 in actual production. To research the performance of vibration isolation quantitatively, another displacement sensor is needed to measure the vibrations in the lab.

D. Compliance Modeling of the Device

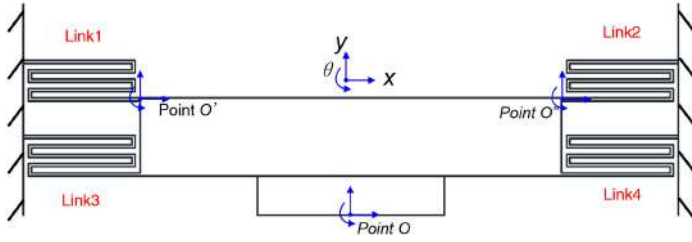In the proposed device, there are two parts of compliant structures. The first one belongs to the active vibration isolation unit and acts as a linear guideway, which is a simple design. The second one is more complex and undertakes the passive vibration isolation mission, whose compliance modeling should be derived in detail.

According to the compliance theory, the force-displacement relationship is shown as:

$$D = C \times F \qquad (1)$$

where D is the displacement vector, C is the compliance matrix, and F is the force vector. The specific expression is:

$$\begin{bmatrix} \triangle x \\ \triangle y \\ \triangle \theta \end{bmatrix} = \begin{bmatrix} C_{x,F_x} & C_{x,F_y} & C_{x,M_z} \\ C_{y,F_x} & C_{y,F_y} & C_{y,M_z} \\ C_{\theta,F_x} & C_{\theta,F_y} & C_{\theta,M_z} \end{bmatrix} \times \begin{bmatrix} F_x \\ F_y \\ M_z \end{bmatrix} \qquad (2)$$

As shown in Fig. 4 and Fig. 5, first $C_{Link1o'Fo'}$ is calculated, which reveals the influence of the force applied to point o' in three directions. The specific expression is

$$C_{Link1o'Fo'} = \sum_{i=1}^{9} T_{di}^9 C_{hingei_i}{}^i T_{f9}{}^i \qquad (3)$$

where $C_{hingei_i}{}^i$ is a 3×3 compliance matrix of each hinge, which is determined by their machine dimensions and material coefficients. And T_{di}^9 is a displacement transformation matrix, which is utilized to transform the displacement that occurred in point i to point 9. $T_{f9}{}^i$ is a force transformation matrix, which is utilized to transform the force applied to point 9 to point i.

$C_{Link1oFo}$ is acquired through a space conversion:

$$C_{Link1oFo} = T_{do'}^o C_{Link1o'Fo'} T_{fo}^{o'} \qquad (4)$$

Based on the symmetry principle, $C_{Link2oFo}$ can be acquired through a space conversion as well:

$$C_{Link2oFo} = T_{do''}^o C_{Link1oFo} T_{fo}^{o''} \qquad (5)$$

Because the connection between link1 and link2 is parallel, so $C_{Link1,2oFo}$ can be acquired by the parallel principle:

$$C_{Link1,2oFo} = \left((C_{Link1oFo})^{-1} + (C_{Link2oFo})^{-1} \right)^{-1} \qquad (6)$$

Due to the similarity of structure, $C_{Link3,4oFo}$ can be acquired by space conversion too:

$$C_{Link3,4oFo} = T_{do'''}^o C_{Link1,2oFo} T_{fo}^{o'''} \qquad (7)$$

Finally, considering that Link 1, 2, 3, and Link 4, the total compliance C_{oFo} is acquired, and the specific expression is:

$$C_{oFo} = \left((C_{Link12oFo})^{-1} + (C_{Link3,4oFo})^{-1} \right)^{-1} \qquad (8)$$

It was found that in the compliance matrix C_{oFo}, as shown in matrix equation (9), all the elements are approximately equal to zero except for the element $C_{y,Fy}$. In addition, a precision slider was utilized to constrain the motion except for the motion along $y-$axis, which makes the other 8 elements in matrix C_{oFo} closer to zero.

$$C_{oFo} = \begin{bmatrix} C_{x,Fx} & C_{x,Fy} & C_{x,M_z} \\ C_{y,Fx} & C_{y,Fy} & C_{y,M_z} \\ C_{\theta,Fx} & C_{\theta,Fy} & C_{\theta,M_z} \end{bmatrix} \qquad (9)$$

E. Device Dynamics Modeling

To satisfy the requirements of the following simulated and experimental verifications of the MAPH vibration isolation strategy, a dynamic model of the designed device was established (see Fig. 3(c)). First, the stiffness of the spring k_2 in Fig. 3(c) can be acquired through

$$k_2 = \frac{1}{C} = \frac{1}{C_{y,Fy}} \qquad (10)$$

The output and input of the passive vibration isolation unit are the position x_2 and x_1, respectively, and the flexure connection can be replaced by a spring and a damping. Therefore, the differential equation acquired through the Newton's second law can be expressed as:

$$m_2 \ddot{x}_2 = k_2 (x_1 - x_2) + c_2 (\dot{x}_1 - \dot{x}_2) \qquad (11)$$

where m_2 means the equivalent mass block of the AFM, which is the target needed to be protected from the vibration. After the Laplace transformation, the transfer function of the passive vibration isolation unit is obtained and can be expressed as:

$$\frac{X_2(s)}{X_1(s)} = \frac{\frac{c_2}{m_2}s + \frac{k_2}{m_2}}{s^2 + \frac{c_2}{m_2}s + \frac{k_2}{m_2}}. \qquad (12)$$

The input and output of the active vibration isolation unit are the voltage signal to the piezoelectric stacks and x_1. The transfer function of the active vibration isolation unit can be simply regarded as 1 because its position output can have a rapid and linear response to the input voltage signal under the closed-loop control.

The last process refers to the VCM. Taking the force of VCM as the input and the position x_2 as the output, the differential equation acquired through Newton's second law can be expressed as:

$$m_2 \ddot{x}_2 = -k_2 x_2 - c_2 \dot{x}_2 + F_{VCM}. \qquad (13)$$

TABLE I
MECHANICAL PROPERTIES OF SEVERAL HIGH-STRAIN MATERIALS

Material	Fatigue stress σ_{Fa} / MPa	E / GPa	Density ρ / (kg/m³)	ε_{Fa} (σ_{Fa}/E)
Ti-6Al-4V	470	113.8	4430	0.0041
AL7075-T6	223	71.7	2810	0.0031
55Si2MnB	720	206.6	7750	0.0034

After the Laplace transformation, the transfer function of the force compensation using a VCM as an actuator is obtained and can be expressed as:

$$\frac{X_2(s)}{F_{VCM}(s)} = \frac{\frac{1}{m_2}}{s^2 + \frac{c_2}{m_2}s + \frac{k_2}{m_2}}. \qquad (14)$$

III. MECHANISM OPTIMIZATION AND FEA ASSESSMENT

After the integrated design of the whole device, to ensure the device has a great vibration isolation performance, the mechanical structure of the passive vibration isolation unit should be optimized by adopting proper material and adjusting dimension parameters. Moreover, some FEA analyses of the optimized mechanism and the effect of the VCM force compensator are presented in this section.

A. Material Selection

Material selection is important for the passive vibration isolation structure. Because the passive vibration isolation works continuously, material fatigue and failure need to be considered first. Therefore, materials with a high ratio of fatigue stress to Young's modulus ε_{Fa} should be adopted. To make the effective vibration isolation region of the passive vibration isolation unit cover more frequencies, the stiffness of the passive vibration isolation unit should be low. However, limited by electro-sparking manufacturing, the thickness of the flexure structure cannot be too thin, which limits the stiffness the passive vibration isolation unit can achieve at a low value. On the other hand, since the flexure structure is suspended in mid-air, the density of the passive vibration isolation should not be too high. The heavy suspended structure may bring about more instability. The mechanical properties of several common materials with high ε_{Fa} value are listed in Table I. From Table I, we can see that, though Ti-6Al-4V and 55Si2MnB own a relatively high ε_{Fa}, their density is far higher than AL7075-T6. Considering Young's modulus has a positive correlation with stiffness, the AL7075-T6 is the most suitable material for this design.

B. Optimization Objectives and Results

As shown in Fig. 4, the main dimensional parameters of the flexure structure of the proposed device are: the length of the flexure hinge $l_1, l_2, l_3, l_4, l_5, l_6, l_7, l_8, l_9$ and the overall thickness t. To simplify the optimization calculation, l_1, l_9 are set as l_a, and l_2, l_4, l_6, l_8 are set as l_b, and l_3, l_5, l_7 are set as l_c. The relationship between l_a, l_b and l_c is:

$$l_c = 2 \times l_a - 30 \times 10^{-3} \qquad (15)$$
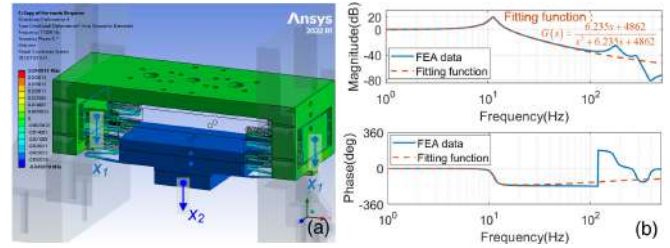
Fig. 6. FEA simulation results of the optimized passive vibration isolation unit of the device. (a) the 3D results when the resonance is aroused (the resonant frequency is 11.098Hz); (b) comparison of frequency responses.

where the distance between two rigid bodies on the left side and the right side is 30 mm. Thus l_a, l_b, and t are chosen as optimization parameters because they play the most important role in passive vibration isolation performance after the material. Then the lower limits of l_a, l_b, t are set as 27, 2.3, and 0.8 respectively, and the upper limits are set as 29, 3, and 1 respectively. To make better use of passive vibration isolation performance, emphasis should be placed on the resonant frequency of the passive vibration isolation unit, and the mass of flexure hinges should be reduced because they are suspended in mid-air.

The optimization task was undertaken by MATLAB using the Pareto method. After several iterations, the optimization dimensions were obtained: l_a = 28.3 mm, l_b = 2.4 mm, t = 0.8 mm, which generates an optimal performance with resonant frequency ω_n = 63.056 rad/s and the volume of the flexure hinge V = 4204.8 mm^3.

C. FEA Simulation and Assessment

The harmonic response of the optimized passive vibration isolation unit was evaluated by ANSYS Workbench. As shown in Fig. 6(a), a displacement input was added to x_1, with an amplitude of 500 nm, and frequency changes from 1Hz to 500Hz. The input x_1 and output x_2 are measured to plot the frequency response. In Fig. 6(b), it can be seen that the passive vibration isolation unit acts like a second-order system(MCK system), which works with the dynamic model derived in Section II. The resonant frequency is about 11.098Hz and is near the optimized result acquired above (63.056 rad/s≈10.04 Hz). As section II stated, the VCM can improve the dynamic performance of position tracking for x_2. The effect of the force compensation provided by VCM is evaluated. As shown in Fig. 7, the rise time of x_2 is decreased by the force compensation of the VCM, which means the dynamic performance of the device is improved by VCM.

IV. DESIGN OF CONTROLLING STRATEGY

In this section, a double compensating PID controller to allow the proposed system work in the method of MAPH vibration isolation is demonstrated.

A. Closed-loop Control Strategy

As shown in Fig. 8, the terminal output is the position x_2. The vibration denoted as d enters the loop from the position x_1. The vibration can be divided into two groups from

Fig. 7. FEA simulation verification of VCM force compensation.

Fig. 8. The control scheme. (a) entire control system; (b) VCM compensator block; (c) passive vibration isolation unit block; (d) active vibration isolation unit block.

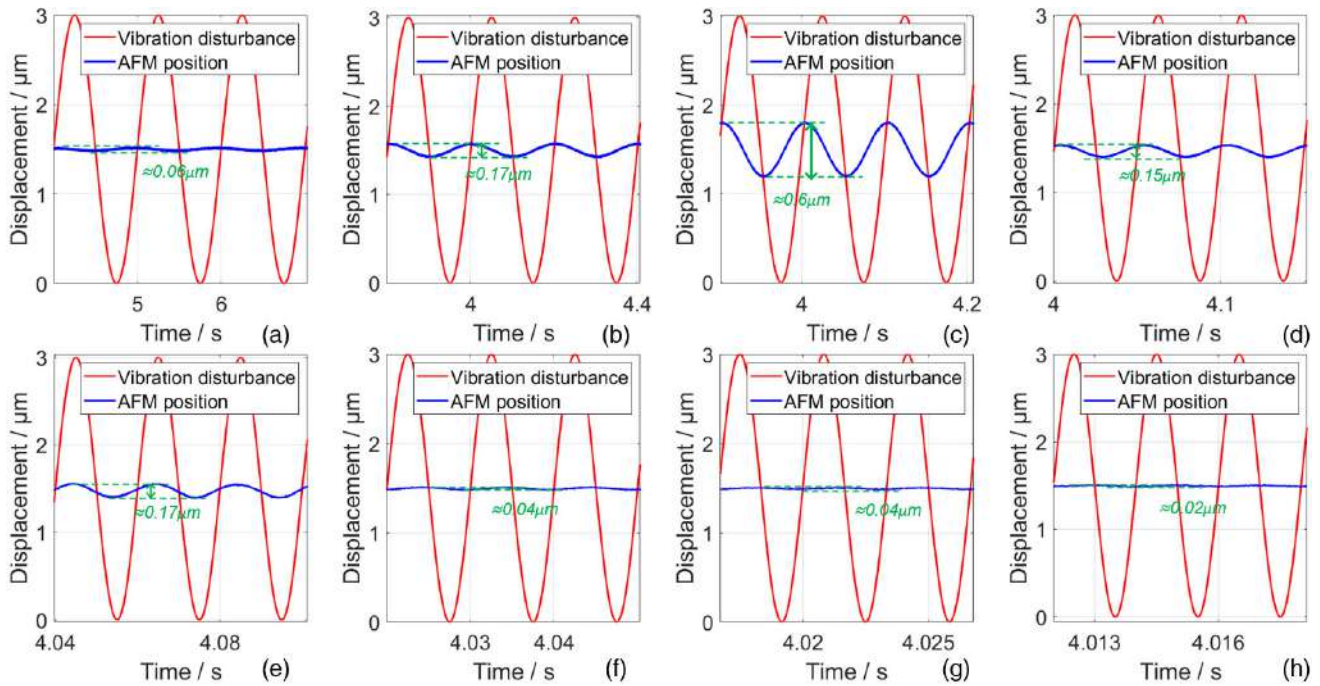the perspective of frequency, i.e., low-frequency and high-frequency vibrations. The criteria for delineating vibrations is if the vibration can be isolated by the passive vibration isolation unit, it is a high-frequency vibration. The other vibration is classified as a low-frequency vibration. The low-frequency vibration is first rejected by the loop around the controller PID3. Then, the remnant vibration on x_1 is merely a high-frequency vibration, which will be dissipated by the passive vibration isolation. For the purposes of the closed-loop control of x_2 and taking x_1 as the process variable and taking x_2 as the control variable, a cascade control was adopted because a long time constant is present between x_1 and x_2. In addition, the controller gain of PID3 can be set at a high value, so the cascade control is achievable. We regard the loop around the controller PID3 as the displacement compensation because the original purpose of this loop is not controlling the position of the AFM scanning head, but compensating for the vibration through reverse displacement.

Besides the displacement compensation, the VCM is added to improve the dynamic performance of the reference tracking for the AFM scanning head because it can apply force directly to the AFM scanning head to compensate for the force shortage of the force caused by low-rigidity connection. Therefore, the ambition of the loop around PID1 is to provide force compensation. A VCM can further stabilize the AFM scanning head. It can eliminate some residual low-frequency vibrations on x_2 resulting from the friction of internal components, such as the slider.

B. Simulation and Assessment

To verify the effectiveness of the designed controller, the entire device is established in the MATLAB Simulink software according to Fig. 8. The input of these simulations is the vibration disturbance (d), and the output is the position of the AFM scanning head (x_2).

To make the simulation more in line with reality, a time delay unit was applied to the active vibration isolation unit, counteracting the low-frequency vibrations. As shown in Fig. 9, the vibration with the same amplitude of 0-3 μm and varying frequencies are applied to the plant as the disturbance. It can be observed that the frequency varies from 1Hz to 500Hz, and the vibration disturbance has been eliminated under this controlling strategy. Even within the resonant frequency range, seeing Fig. 9 (c), the vibration amplification phenomenon has been

significantly suppressed. The simulation results successfully verified the effectiveness of the designed controlling strategy.

V. EXPERIMENTAL VERIFICATION AND DISCUSSION

In this section, to generate vibration disturbances, an auxiliary mechanism was first designed and demonstrated. Then the prototype system was established. A series of experimental tests, including vibration isolation tests, the closed-loop positioning test and the stability maintenance test were conducted to verify the superiority of the proposed self-stabilization nanopositioning device.

Fig. 10. Diagram of the auxiliary mechanism (blue parts). (a) oblique drawing; (b) right side drawing.

Fig. 11. Experimental setup. (1) PZT voltage amplifier, (2) dSPACE system, (3) AFM scanning head equivalent load, (4) S-shape flexure hinge (passive vibration isolation unit), (5) active vibration isolation unit (including piezoelectric stack actuators), (6) VCM, (7) cylindrical PZT actuators, (8) auxiliary mechanism.

A. Establishment of Experimental System

An auxiliary mechanism is designed and presented in Fig. 10 (the blue section). The mechanism uses the cylindrical PZT and the flexure plate-form spring (linear guideway) to generate controllable and measurable vibration disturbances along the z-axis.

Fig. 9. Simulation results of vibration isolation performances at the same amplitude (3μm) and different frequencies. (a) 1Hz; (b) 5Hz; (c) 10Hz; (d) 20Hz; (e) 50Hz; (f) 100Hz; (g) 300Hz; (h) 500Hz.

The experimental system (symmetric distributed) is displayed in Fig. 11, AL 7075-T651 material was adopted to fabricate the prototype (particularly the flexure structure) via the WEDM machining technics, and a small part is made of steel. A precision linear guideway (VRT1025) is utilized to limit the foundational support of the AFM scanning head equivalent load to one degree of freedom. On each side, there is a cuboid shape PZT stack (Pst150/7x7/20) to actuate the active vibration isolation unit to implement displacement compensation. The vibration disturbance is generated by the auxiliary mechanism and driven by the cylindrical PZT (XMTPSt150/7/40VS12). At the very top, a VCM (TMEC0001-001-00A) is utilized to provide force compensation. Outside of the device, controller implementation was achieved by using the dSPACE rapid prototyping simulating system (DS-1007, dSPACE), while the displacement sensor model is NS-DCS10L-430F.

B. Vibration Isolation Tests of the Nanopositioning Device

Before implementing the vibration isolation test, the magnitude response of the passive vibration isolation was verified first because it is an open-loop process that can hardly be improved with control. As shown in Fig. 12, the experimental magnitude response shows that the resonant frequency is about 11Hz and the experimental magnitude response is consistent with the magnitude response of the FEA result and fitting function, which certifies the effectiveness of the passive vibration isolation unit.

Based on the superposition theorem of the linear system and for simplicity, a series of representative frequency points were selected to illustrate the MAPH vibration isolation performance. The initial point at 1Hz was selected because the passive vibration isolation unit cannot mitigate low-frequency vibration. The second point at 10Hz was selected because the passive vibration isolation unit will even exhibit vibration
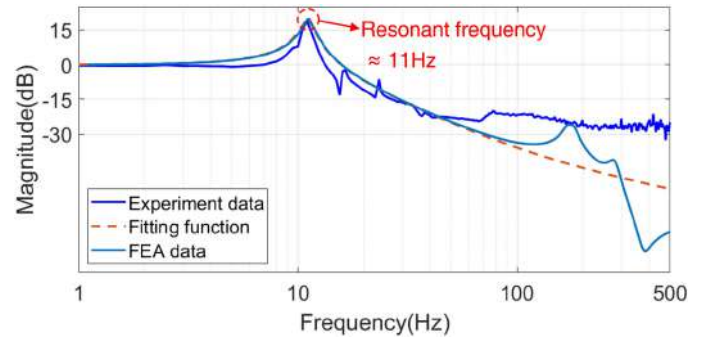

Fig. 12. Magnitude response of the passive vibration isolation unit.

amplification within the resonant range and the third point at 20Hz was selected because the passive vibration isolation unit starts to take effect, as seen from the magnitude response curve in Fig. 12, while this frequency is not too harsh for the active vibration isolation. As for the remaining two frequency points (40Hz and 80Hz), the passive vibration isolation unit can eliminate the vibration with a frequency over twice the resonant frequency. However, the active vibration isolation unit also has to confront a greater challenge mainly resulting from the sensor delay, and the driving capability of the actuator.

As shown in Fig. 10, the vibration disturbance (d) generated by the auxiliary mechanism mentioned in the previous section acts on the rigid top surface directly as Fig. 1 and Fig. 3 illustrate. The amplitude of d is about $\pm 5\mu$m, and the frequencies are located on the series of representative frequency points above. The input d and the output x_2 are measured to present the vibration performance of the whole device and the MAPH strategy. It can be observed that at 1Hz, the passive vibration isolation unit is completely unable to eliminate the vibrations, while the proposed strategy eliminates 97% of
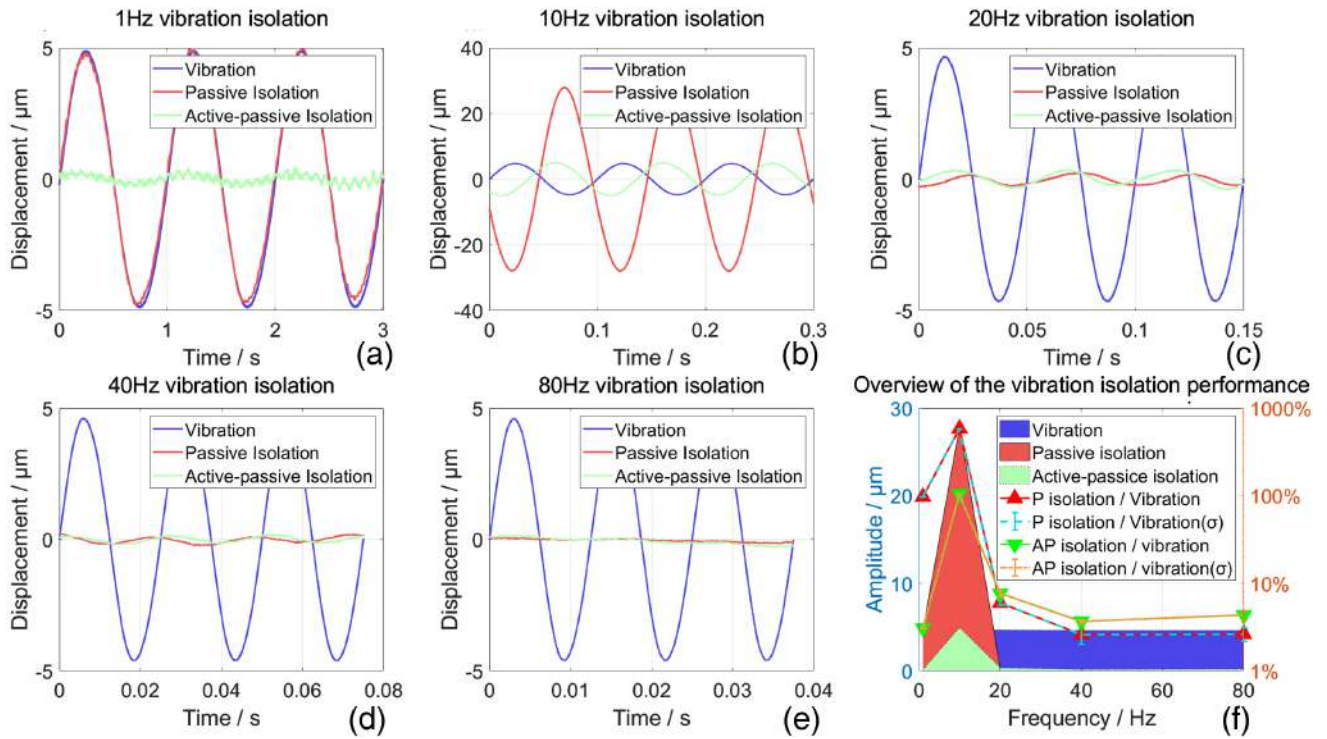
Fig. 13. Vibration isolation performance test under vibration disturbances of the same amplitude and different frequencies. (a) 1Hz; (b) 10Hz; (c) 20Hz; (d) 40Hz; (e) 80Hz; (f) frequency-domain overview of the vibration isolation performance.

vibrations, which results in the output position fluctuations are kept within $\pm 0.15 \mu$m. As Fig. 13 (b) shows, the amplitude of the vibration at the frequency of 10Hz (within the resonant range) passed the passive vibration isolation unit becomes relatively large (5.85 times larger than the initial vibration disturbance). However, the MAPH strategy has suppressed the vibrations caused by the passive vibration mechanism (much less than the 5.85 times one). Looking at Fig. 13(c)-(e), with vibrational frequencies at 20Hz, 40Hz, and 80Hz, the passive vibration isolation unit and the MAPH isolation strategy worked as intended. With the improvement of the frequency of the vibration disturbance from 80Hz, as shown in Fig. 12, the displacement transmissibility is decaying in general and maintained at a level less than -20dB. Meanwhile, the proposed MAPH vibration isolation strategy has almost no negative effects on passive vibration isolation. The vibration at the frequency within 80Hz-500Hz can also be generally eliminated just like Fig. 13(d) and Fig. 13(e) present.

C. Closed-loop Positioning Performance Test

Except for the vibration isolation task, reference tracking performance is important in practical production. Thus, a VCM is added to the device to improve its performance. As shown in Fig. 14, we can observe that using both the PZT stack and VCM as the actuator, the response speed becomes faster and the steady-state error is eliminated because the VCM has provided a controlled force to compensate for the insufficient force that the target tracking reference needed, and the PZT stack provides a high precision balance point attracting the target to arrive to the desired point.

On the other hand, seeing the comparison in Fig. 14(b), the control variable remains high level (which is positively

related to the force) under the circumstances actuated only by the VCM, which means the VCM is continuously pushing and pulling the output. In this case, the VCM easily becomes charred due to the overheating problem during actual operations. On the contrary, the control variable of VCM under the circumstances actuated by both VCM and PZT stack remains low level, when the AFM scanning head arrives at the right place. According to Ampere's rule, the relationship between heat production and the control variables is demonstrated as follows:

$$F = BIL = Kv \tag{16}$$

$$I = F/(BL) \tag{17}$$

$$q = I^2 R = F^2/(BLR) \tag{18}$$

$$Q = \int q\,dt = BLR \times \int F^2\,dt = K^2 BLR \times \int v^2\,dt \tag{19}$$

where F represents the driving force generated by the VCM, B represents the invariant magnetic flux density, I represents the current following in the coil, v represents the control variable shown in Fig. 14b), K is a positive coefficient; q and Q represent the transient heating production and the cumulative heating production, respectively. It is obvious that by using the VCM and PZT stack as the actuator with the MAPH vibration isolation strategy, the damage to the VCM caused by overheating can be avoided.
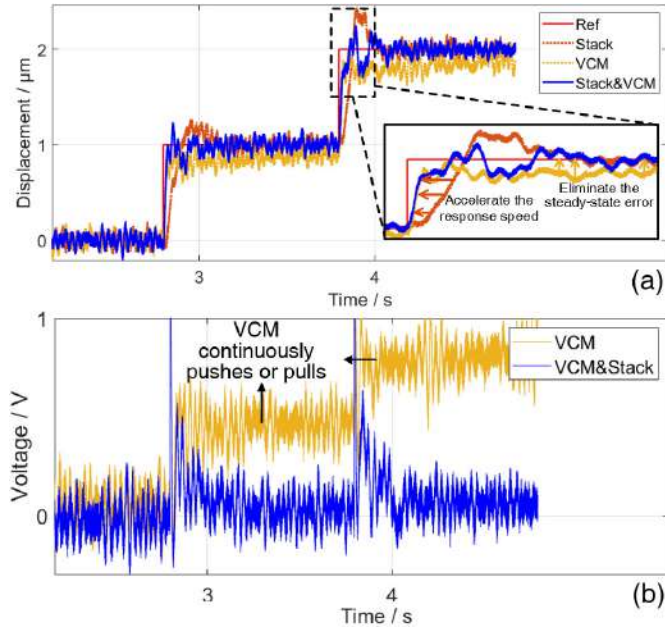
Fig. 14. Tracking performance improvement. (a) Closed-loop tracking under different driving modes; (b) comparison of control signal of VCM under different driving modes.

D. Stability Maintenance Test

Subsection B has presented the frequency-domain vibration isolation performance of the nanopositioning device that has adopted the MAPH vibration isolation strategy. Based on the superposition principle of the linear system, the nanopositioning device can perform complex vibration elimination well. To further validate the vibration eliminating performance in the practical production facing the aperiodic vibration disturbance, the step change signal was adopted as the simulated disturbance signal because the step signal is always utilized to test the linear time-invariant (LTI) system and can provide an intense disturbance to validate system stability performance. As shown in Fig. 15, the step changes vibration disturbance represented by the red solid line changes within $\pm 2.35 \mu m$ and we can observe that, although facing intense disturbances, the nanopositioning device using a MAPH vibration isolation strategy remains stable. Mostly, the target position is kept within $\pm 0.3 \mu m$. Moreover, the steady-state positioning accuracy of the device achieves $\pm 0.1 \mu m$ and the attenuation ratio of the disturbances achieved up to 70%.

E. Performance Evaluation and Discussion

To validate the effectiveness of the proposed nanopositioning device with the MAPH vibration isolation strategy, we compared it to existing devices with the traditional APH vibration isolation strategy described in [28]–[31]. The steady-state precision, load capacity, and working frequency are the typical quantities used to characterize the performance of the nanopositioning device with a vibration isolation function. For a clear comparison, several typical devices are tabulated in Table II. Although the device described in [28] has a better steady-state precision and wider working frequency than ours, its load capacity of 0.1 kg is insufficient to support the weight of the AFM. On the other hand, our proposed
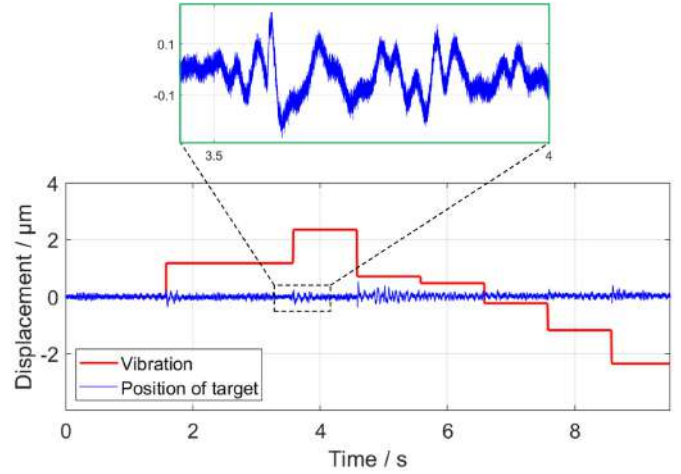
device surpasses the devices of [29] and [31] in both load capacity and working frequency. Meanwhile, the devices in [29] and [32] may have a larger load capacity, but it cannot provide a stable working environment for the AFM, because of their lack of precise closed-loop positioning control. To summarize, this work with the MAPH vibration isolation strategy is capable of simultaneously achieving high steady-state precision ($\pm 0.1 \mu m$) and high load capacity (2.5kg) and large working frequency (500Hz).

In addition, it is worthwhile to mention that, the vibration isolation performance within the narrow resonant frequency range is not as good as the performance in the other regions of the working frequency. However, the performance can be further improved by enhancing resistance to yield and fatigue failure with optimization algorithm [33] and by adopting more progressive controlling strategy simultaneously [34].

Fig. 15. Aperiodic vibration disturbance eliminating performance test.

TABLE II
PERFORMANCE COMPARISON OF THE VIBRATION ISOLATION DEVICE

	Steady-state precision	Load capacity	Actuator	Working frequency
[28]	$\pm 0.01 \mu m$	<0.1kg	Lorentz actuator	$\leq$ 5kHz
[29]	-	20kg	VCM	$\leq$100Hz
[30]	$\pm 0.6 \mu m$	1.4kg	VCM	$\leq$ 380Hz
[31]	$\pm 2 \mu m$	2kg	PZT&VCM	$\leq$ 100Hz
[32]	-	3kg	Magnetostrictive actuator	60-150Hz
This work	$\pm 0.1 \mu m$	**2.5kg**	**PZT&VCM**	$\leq$ **500Hz**

VI. CONCLUSIONS

A compliant self-stabilization device with the MAPH vibration isolation strategy is proposed and validated in this paper. The main achievements are:

1) A flexure-based vibration isolation device with dual compensators (PZT & VCM), and a novel MAPH vibration isolation strategy were developed, respectively;

2) A DCPID closed-loop controlling strategy aiming at making the proposed device work in the method of MAPH vibration isolation is presented;

3) A series of validation experiments were successfully conducted. The frequency-domain vibration isolation rates out of the resonance region ($\leq$500Hz) can achieve 90% or more. Its steady-state positioning accuracy achieved $\pm$ 0.1 μm, load capacity achieved up to 2.5kg, and the attenuation ratio of the disturbances achieved up to 70%. Also, the problem of VCM overheating has been avoided.

The results comprehensively confirm that the proposed device can provide a stable and reliable working environment for the AFM scanning head and lays the foundation for the surface physical property inspection system for Micro/mini LED display panels. As for the future, the developed compliant self-stabilization nanopositioning device will be integrated into the industrial AFM inspection equipment to undergo practical sample testing under a production-line environment.

REFERENCES

[1] P. R. Ouyang, W. J. Zhang, M. M. Gupta, and W. Zhao, "Overview of the development of a visual based automated bio-micromanipulation system," *Mechatronics*, vol. 17, no. 10, pp. 578-588, Dec. 2007.

[2] K. Y. Woo, H. G. Song, K. Lee, Y. C. Sim, and Y.H. Cho, "Influence of wafer quality on chip size-dependent efficiency variation in blue and green micro light-emitting diodes," *Sci. Rep.*, vol. 12, no. 1, Dec. 2022.

[3] R. Koutavarapu, R. K. N. R. Manepalli, B. T. P. Madhav, M. C. Rao, and J. Shim, "Structural, optical and magnetic properties of Cd doped ZnO nanomaterials for optoelectronic device application," *J. Mater. Sci. Mater. Electron.*, vol. 32, no. 8, pp. 11264-11273, Apr. 2021.

[4] S. Ito and G. Schitter, "Atomic force microscopy capable of vibration isolation with low-stiffness Z-axis actuation," *Ultramicroscopy*, vol. 186, pp. 9-17, Mar. 2018.

[5] T. D. Le, M. T. N. Bui, and K. K. Ahn, "Improvement of vibration isolation performance of isolation system using negative stiffness structure," *IEEE/ASME Trans. Mechatron.*, vol. 21, no. 3, pp. 1561-1571, Jun. 2016.

[6] A. Carrella, M. J. Brennan, and T. P. Waters, "Static analysis of a passive vibration isolator with quasi-zero-stiffness characteristic," *J. Sound Vib.*, vol. 301, no. 3-5, pp. 678-689, Apr. 2007.

[7] EI Rivin, "Passive Vibration Isolation," *Appl. Mech. Rev.*, vol. 57, no. 6, pp. B31-B32, Nov. 2004.

[8] J. Li, Z. Li, X. Jing, and X. Huang, "Fuzzy adaptive tracking control for nonlinear suspension systems based on a bio-inspired reference model," *Proc. World Congr. Intell. Control Autom.*, vol. 2018-July, pp. 119-124, Jan. 2019.

[9] X. Wang, F. Bi, and H. Du, "Reduction of low frequency vibration of truck driver and seating system through system parameter identification, sensitivity analysis and active control," *Mech. Syst. Signal Process.*, vol. 105, pp. 16-35, May 2018.

[10] J. Ding, X. Luo, X. Chen, O. Bai, and B. Han, "Design of active controller for low-frequency vibration isolation considering noise levels of bandwidth-extended absolute velocity sensors," *IEEE/ASME Trans. Mechatron.*, vol. 23, no. 4, pp. 1832-1842, Aug. 2018.

[11] C. Chen, Z. Liu, Y. Zhang, C. L. P. Chen, and S. Xie, "Actuator backlash compensation and accurate parameter estimation for active vibration isolation system," *IEEE Trans. Ind. Electron.*, vol. 63, no. 3, pp. 1643-1654, Mar. 2016.

[12] T. B. Airimitoaie and I. D. Landau, "Robust and adaptive active vibration control using an inertial actuator," *IEEE Trans. Ind. Electron.*, vol. 63, no. 10, pp. 6482-6489, Oct. 2016.

[13] Y. Jia, H. Tang, S. Xu, Y. Xu, X. Chen, and Y. Tian, "A novel decoupled flexure nanopositioner with thermal distortion self-elimination function," *IEEE/ASME Trans. Mechatron.*, vol. 27, no. 5, pp. 2953-2962, Oct. 2022.

[14] S. Ito, J. Steininger, and G. Schitter, "Low-stiffness dual stage actuator for long rage positioning with nanometer resolution," *Mechatronics*, vol. 29, pp. 46-56, Aug. 2015.

[15] H. Tang et al., "Development and repetitive-compensated pid control of a nanopositioning stage with large-stroke and decoupling property," *IEEE Trans. Ind. Electron.*, vol. 65, no. 5, pp. 3995-4005, May 2018.

[16] W. Sun, H. Gao, and O. Kaynak, "Vibration isolation for active suspensions with performance constraints and actuator saturation," *IEEE/ASME Trans. Mechatron.*, vol. 20, no. 2, pp. 675-683, Apr. 2015.

[17] H. Tang, S. He, et al., "A monolithic force sensing integrated flexure bonder dedicated to flip-chip active soft-landing interconnection," *IEEE/ASME Trans. Mechatron.*, vol. 26, no. 1, pp. 323-334, Feb. 2021.

[18] W. Sun, Z. Zhao, and H. Gao, "Saturated adaptive robust control for active suspension systems," *IEEE Trans. Ind. Electron.*, vol. 60, no. 9, pp. 3889-3896, 2013.

[19] J. Hong and K. Park, "Design and control of six degree-of-freedom active vibration isolation table," *Rev. Sci. Instrum.*, vol. 81, no. 3, p. 035106, Mar. 2010.

[20] J. Zhao et al., "Shock isolation capability of an electromagnetic variable stiffness isolator with bidirectional stiffness regulation," *IEEE/ASME Trans. Mechatron.*, vol. 26, no. 4, pp. 2038-2047, Aug. 2021.

[21] L. Tu et al., "Semiactively controllable vehicle seat suspension system with negative stiffness magnetic spring," *IEEE/ASME Trans. Mechatron.*, vol. 26, no. 1, pp. 156-167, Feb. 2021.

[22] Y. Sun et al., "High-Static-Low-Dynamic stiffness isolator with tunable electromagnetic mechanism," *IEEE/ASME Trans. Mechatron.*, vol. 25, no. 1, pp. 316-326, Feb. 2020.

[23] Y. H. Shin, T. Y. Kim, B. C. Jung, S. J. Moon, and J. H. Lee, "Development of hybrid vibration isolator by inertial-type actuator and wire mesh mount," *IEEE/ASME Trans. Mechatron.*, vol. 24, no. 3, pp. 1356-1367, Jun. 2019.

[24] B. Yan, H. Ma, W. Zheng, B. Jian, K. Wang, and C. Wu, "Nonlinear electromagnetic shunt damping for nonlinear vibration isolators," *IEEE/ASME Trans. Mechatron.*, vol. 24, no. 4, pp. 1851-1860, Aug. 2020.

[25] D. Ning, H. Du, S. Sun, W. Li, and W. Li, "An energy saving variable damping seat suspension system with regeneration capability," *IEEE Trans. Ind. Electron.*, vol. 65, no. 10, pp. 8080-8091, Oct. 2018.

[26] M. Amjadian and A. K. Agrawal, "A passive electromagnetic eddy current friction damper (PEMECFD): Theoretical and analytical modeling," *Struct. Control Heal. Monit.*, vol. 24, no. 10, p. e1978, Oct. 2017.

[27] W. J. Zhang, P. R. Ouyang, and Z. H. Sun, "A novel hybridization design principle for intelligent mechatronics systems," *Abstr. Int. Conf. Adv. mechatronics Towar. Evol. fusion IT mechatronics ICAM*, vol. 2010.5, no. 0, pp. 67-74, 2010.

[28] S. Ito and G. Schitter, "Comparison and classification of high-precision actuators based on stiffness influencing vibration isolation," *IEEE/ASME Trans. Mechatron.*, vol. 21, no. 2, pp. 1169-1178, Apr. 2016.

[29] M. H. Kim, H. Y. Kim, H. C. Kim, D. Ahn, and D. G. Gweon, "Design and Control of a 6-DOF active vibration isolation system using a halbach magnet array," *IEEE/ASME Trans. Mechatron.*, vol. 21, no. 4, pp. 2185-2196, Aug. 2016.

[30] E. Csencsics, M. Thier, R. Hainisch, and G. Schitter, "System and control design of a voice coil actuated mechanically decoupling two-body vibration isolation system," *IEEE/ASME Trans. Mechatron.*, vol. 23, no. 1, pp. 321-330, Feb. 2018.

[31] B. Zhao, W. Shi, and J. Tan, "Design and control of a dual-stage actuation active vibration isolation system," *IEEE Access*, vol. 7, pp. 134556-134563, 2019.

[32] X. Sun, Y. Liu, W. Hu, T. Sun, and J. Hu, "Design optimization of a giant magnetostrictive driving system for large stroke application considering vibration suppression in working process," *Mech. Syst. Signal Process.*, vol. 138, p. 106560, Apr. 2020.

[33] L. Cao, A. T. Dolovich, A. Chen, and W. (Chris) Zhang, "Topology optimization of efficient and strong hybrid compliant mechanisms using a mixed mesh of beams and flexure hinges with strength control," *Mech. Mach. Theory*, vol. 121, pp. 213-227, Mar. 2018.

[34] H. Zhang, X. Zhao, H. Wang, G. Zong, and N. Xu, "Hierarchical sliding-mode surface-based adaptive actor-critic optimal control for switched nonlinear systems with unknown perturbation," *IEEE Trans. Neural Networks Learn. Syst.*, 2022.

Zhongyuan Zhu was born in Guangdong, China, in 1998. He received the B.Sc. degree from the school of Electromechanical Engineering in Guangdong University of Technology, Guangzhou, China, in 2020, where he is currently working towards the M.S. degree in mechanical engineering.

His research interests include flexure-based compliant mechanism, nanopositioning control, and industrial-level AFM scanning, display panel inspection equipment applications.

Zhihang Lin received his Ph.D degree in mechanical engineering from Tsinghua University, Beijing, China, in 2020. He is currently a Lecturer and "Youth 100 Plan Talent" with the School of Electromechanical Engineering, Guangdong University of Technology, Guangzhou, China. From 2020 to 2021, he was a research fellow with the Jihua laboratory in Foshan, Guangdong. He has served as reviewer of many well-known conferences such as IEEE/ASME International Conference on Advanced Intelligent Mechatronics (AIM) and has published many SCI/EI academic papers.

His interests include compliant connection mechanism, thermal/vibration error detection and compensation, advanced LED packaging equipment applications.

Hui Tang (Member, IEEE) received the Ph.D degree in electromechanical engineering from the University of Macau, Macao, China, in 2014. He has been the Marie Curie Research Fellow with Warwick University, Coventry, U.K., since 2022. From 2016 to 2018, he was a Postdoctoral Fellow with the Columbia University, New York, NY, USA, and The Hong Kong Polytechnic University, Hong Kong. He is also a Professor and A+ Youth 100 Plan Talent with the School of Electromechanical Engineering, Guangdong University of Technology, Guangzhou, China. He has authored or coauthored 80 peer-reviewed SCI/EI academic papers including high-ranking journals such as IEEE TRANSACTIONS ON INDUSTRIAL ELECTRONICS, IEEE TRANSACTIONS ON INDUSTRIAL INFORMATICS, IEEE/ASME TRANSACTIONS ON MECHATRONICS, and IEEE TRANSACTIONS ON ROBOTICS. Dr. Tang has served as a Reviewer for many well-known SCI journals and conferences such as IEEE transactions, ICRA, etc. He has also served as an Associate Editor for the IEEE/RSJ International Conference on Intelligent Robots and Systems and has chaired several well-known conference sessions (IROS, 3M-NANO, and ICIRA).

His interests include flexure-based compliant mechanism, nanopositioning control, micro/nano manipulations, and Mini/MicroLED mass transfer equipment development.

Yanling Tian received the Ph.D. degree in mechatronics engineering from Tianjin University, Tianjin, China, in 2005. He is an Associate Professor with the School of Engineering, University of Warwick, Coventry, U.K. Prior to joining Warwick University, he held the Research Fellowship with Monash University, Melbourne, Australia, Alexander von Humboldt Fellowship for Experienced Researchers with Oldenburg University, Oldenburg, Germany, and Marie Curie Fellowship with Warwick University. He is the Fellow of Higher Education Academy (FHEA), Heslington, U.K. He has authored or coauthored more than 200 high-ranking journals and peer-reviewed conference papers. His research interests include micro/nano robotics and automation, precision instrument design and modeling and control, metrology and characterization, and mechanobiology and biomechanics.

Dr. Tian was a Technical Editor for IEEE-ASME TRANSACTIONS ON MECHATRONICS from 2015 to 2020.
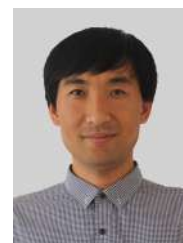
Peng Yu received both his B.Eng. degree in 2002 and M.S. degree in 2005 in Marine Engineering from Dalian Maritime University, China. Now he is an associate Professor in the State Key Laboratory of Robotics, Shenyang Institute of Automation, Chinese Academy of Sciences, Shenyang, China.

His research interests include AFM and nanomanipulation robot.

Yunwei Huang received his B.Sc. degree in Mechanical Manufacturing and Automation from Beibu Gulf University Qinzhou, China, in 2020. He is currently working toward the M.S. degree in mechanical engineering in the Guangdong University of Technology, Guangzhou, China.

His research interests include micro/nano positioning system, advanced alignment control, and Mini/MicroLED mass transfer equipment development.

Chanmin Su received his Ph.D in solid-state physics from the Chinese Academy of Sciences in 1988. He is currently a professor at the State Key Laboratory of Robotics, Shenyang Institute of Automation Chinese Academy of Sciences, Shenyang, China.

His research interests include AFM, micro/nano systems, and nanobiotechnology.